International Journal of Concrete Structures and Materials

RESEARCH

Open Access

Behavior of Reinforced Concrete Circular Columns Subjected to Double Curvature Buckling Moment

Ahmed Hamoda[1*], Sabry Fayed[1*], Walid Mansour[1] and Mohamed Emara[2,3]

Abstract

This paper investigates experimentally and numerically structural performance of reinforced concrete (RC) circular column under double curvature buckling moment. RC circular columns are popularity embraced in RC structures not only owing to its esthetic, attractive appearance and easy for construction, but also for its better contribution for stress resistance. However, the corner or edge columns may be exposed to edge moment (EM) transferred from beam–column joint with double curvature effect. The current investigation proposes to understand the structural exhibition of such columns subjected to double curvature buckling edge moment generated at beam–column joint considering some parameters. A total number of 11 full-scale RC circular columns were constructed, installed, and then tested up to failure studying four parameters. These parameters were: clear height-to-diameter ratio (λ), longitudinal and lateral steel ratios (μ and ρ, respectively) and concrete type. The λ ratio has been introduced with: 4.89, 4.51 and 4.14. The μ ratio has been presented by: 2.2%, 2.3%, 2.6%, and 3.1%, while the ρ ratio was employed with: 0.84%, 0.93%, 1.00% and 1.18%. Three concrete types were studied; one of them was normal concrete (NC), while the other ones were high-performance concretes (HPCs) which were engineered cementitious composite (ECC) and high-strength fiber reinforced concrete (HSFRC). Experimental outcomes revealed that all studied parameters could affect and upgrade the structural performance; however, both longitudinal reinforcement and height-to-diameter ratio provided significant enhancement (about 51%–64%). Parallel to those exploited experimentally, nonlinear three-dimensional finite element models (FEMs) were installed, executed and established considering experimental outcomes producing an acceptable model with an under/over-estimation of about 4%.

Keywords Circular columns, Reinforcement ratio, Double curvature buckling moment, Finite element simulation, High-performance concrete

1 Introduction

Reinforced concrete (RC) columns are essential structural elements in the load-carrying regime resisting gravity and lateral forces. Circular columns are widely used in public constructional structures because of several structural advantages. Considering such an indispensable part in RC buildings, additional excessive stresses followed by its deterioration may portend to sudden collapsing for the whole structure (Lamberti & Razaqpur, 2024; Taherirani et al., 2022). Recently, several structural elements made of high-performance concretes (HPCs) have been widely utilized in vital structures such as:

Journal information: ISSN 1976-0485/eISSN 2234-1315.

*Correspondence:
Ahmed Hamoda
ahmed_hamoda@eng.kfs.edu.eg
Sabry Fayed
sabry_fayed@eng.kfs.edu.eg
[1] Department of Civil Engineering, Faculty of Engineering, Kafrelsheikh University, Kafrelsheikh 33511, Egypt
[2] Structural Engineering Department, Faculty of Engineering, Zagazig University, B. O. Box 44519, Zagazig, Sharkia, Egypt
[3] Department of Civil Engineering, Delta Higher Institute for Engineering and Technology, Talkha, Egypt

malls, multi-story car parking, high-rise buildings, RC bridges stadiums and covered halls (Dharmaraj et al., 2022; Du et al., 2022; Hamoda et al., 2021). However, such elements may be affected by the vulnerability when exposed to non-designed bending moment. The effect of additional double curvature moment on slender RC circular columns may result in unexpected lateral cracks. Consequently, such non-designed defects may diminish the cross-sectional capacity, especially slender ones, required for resisting gravity loads. Moreover, the generated lateral deformation may lead to forming non-desired imperfection and consequently unexpected premature collapse. Circular columns existed at multi-story buildings are subjected to external rotational moment emanating from that moment created at the beam–column joint. This may lead to form critical double curvature buckling moment that has to be studied for slender column (Hamoda et al., 2023a; Ju & Kwak, 2021; Li et al., 2023; Štefan et al., 2019). Generally, the designers are challenged by obtaining the smallest column's cross-sectional area with better cracking feature and larger load-carrying capacity. Also, capturing the ductile mode is highly required for circular columns in particular with the presence of additional moment might increase the criticality (Abdulla, 2020; Al-Rousan & Barfed, 2019; Jin et al., 2018). Most of previous studies deal with geometric and material variables affecting the structural behavior when subjected to axial loadings (Abdelazim et al., 2020; El-Kholy et al., 2023; Sae-Long et al., 2019). Contextually, the current study explores the influence of geometric properties, reinforcement size and the concrete types which were almost the very significant factors RC columns depend on.

Several researches have been carried out experimentally and numerically in order to explore the structural capacity of circular columns under bending moment (Barua et al., 2021; Chen et al., 2021; Lin et al., 2022). Ghoroubi et al. (Ghoroubi et al., 2020) studied structural performance of 50% damaged RC columns with height-to-diameter (H_e/D_c) ratio (λ) close to 11.5 retrofitted with carbon fiber-reinforced polymer (CFRP) strips. This research aimed to capture the adequate retrofitting configurations for increasing the axial ultimate amplitude, stiffness, ductility beside energy dissipation. Results showed that the applied technique has increased the initial stiffness by about 45%–53%. Aules et al. (2020) developed a novel anchorage regime for strengthening of long RC columns with externally bonded CFRP. The results confirmed that the lateral confinement strengthening augmented the ductility with poor effect on moment and stiffness. However, the resistance moments, stiffness as well as the ductility have been augmented when suing longitudinal CFRP sheets anchored to the RC base through a novel proposed system confined with lateral ones CFRP sheets.

Ratio of both longitudinal and lateral reinforcement together with the slenderness ratio proved to have an intelligible reflection on the structural capacity of slender RC columns (Ahmed et al., 2023a; Alajarmeh et al., 2020; Guo et al., 2021; Hamoda et al., 2023b; Kharal & Sheikh, 2020; Rivera et al., 2021). Ye et al. (2020) provided an experimental investigation on the performance of long RC columns subjected to horizontal static or impact force. Fourteen RC columns were experimented investigating three parameters: slenderness ratio, the longitudinal steel ratio, besides the force value of compression force. Columns with longitudinal reinforcement ratio of 1.4% showed that the residual resistance of the impact damaged specimens decreased remarkably by about 7%–14%. Liu et al. (2023) performed and experimental work on RC columns reinforced eccentrically loaded and reinforced with both steel and basalt fiber-reinforced polymer (BFRP) bars. A set of series consisting of ten long columns were constructed and experimented, comprising six hybrid-RC specimens, two RC columns reinforced with steel bars and two RC counterparts reinforced with BFRP bars. The parameters were (Liu et al., 2023): reinforcement type, eccentricity value of the loading, and ratio of reinforcement. The ultimate capacity for 150 mm eccentric force was diminished by about 53%–55% compared to those rivals with 80 mm eccentricity. Also, the stiffness decreased with the increase of the eccentricity value by about 35%.

Although comprehensive researches have studied the structural behavior of RC circular columns under axial compression forces, the effect of edge moment (EM) transferred from beam–column joint with double curvature effect has yet to be investigated. The exposure to additional unexpected EM may result in critical consequences that could critically affect the column's main job which is carrying the gravity loads. Therefore, the effect of additional EM generated by beam's floor should be considered when designing RC columns. The RC columns highly depend on concrete type, reinforcement ratio and the boundary conditions as previously reported (Ahmed et al., 2023b; Teoh et al., 2023). Therefore, the selected parameters herein related to: geometric properties, reinforcement size and the concrete types which were almost the very sensitive and essential factors of RC columns.

This study focused on investigating the structural exhibition of RC circular columns under double curvature EM generated at beam–column joint. A total number of 11 full-scale RC circular columns were experimented up to failure studying some factors, i.e., clear height-to-diameter ratio (λ), longitudinal and lateral steel ratios

(μ and ρ, respectively), along with concrete type which were normal concrete (NC), engineered cementitious composite (ECC) and high-strength fiber reinforced concrete (HSFRC). The experimental outcomes have been reutilized for installing nonlinear three-dimensional finite element model (FEM) which was then compared and established against experimental results generating model could accurately estimate moment resistance of such columns. The ultimate goal is to explore the effectiveness of the selected factors on RC circular corner or edge columns in both elastic and plastic stages that are very essential for designing and pre-collapsing, respectively. To achieve that, both cracking characteristics and elastic stiffness were recorded, compared and analyzed when studying the elastic criteria. Moreover, the ultimate capacity and energy consumed were delivered for impressing the nonlinear performance. The use of new generations of HPCs in developing high-performance circular columns (in terms of improved resistance, elasticity, durability and absorbed energy) is a novel approach and the outcomes will definitely help engineers and designers in exploring the structural performance of circular edge columns in the construction field.

2 Experimental Program

2.1 General Detail of Tested Columns

A set of 11 RC circular columns were manufactured, instrumented and then loaded by rotational edge moment at the mid-height causing double curvature moment simulated to that transferred from slab's beam in multi-story building. All columns had the same geometric properties which were 150 and 1500 mm for overall diameter and a height, respectively. However, four factors were studied, i.e., clear height-to-diameter ratio, longitudinal and lateral steel ratios and the concrete type. The clear height-to-diameter ratio has been introduced with λ: 4.89, 4.51 and 4.14. The longitudinal steel bars have been represented with ratio computed as area of longitudinal reinforcement to that of concrete section ($\mu = A_{st}/A_c$): 2.2%, 2.3%, 2.6%, and 3.1%. The closed circular stirrups were used with volume ratio calculated as the volume for one stirrup to that of the confined concrete between two stirrups ($\rho = V_{st}/V_c$): 0.84%, 0.93%, 1.00% and 1.18%. Three concrete types were studied: one of them was NC, while the other two types were emanated from HPCs families which were: ECC and HSFRC. The major motive for height-to-diameter ratio (i.e., λ) is to determining whether a column may collapse by buckling or can safely resist the gravity forces (Afefy & El-Tony, 2016; Aules et al., 2020; Chen et al., 2021; Taherirani et al., 2022). The significance of steel ratios (i.e., μ and ρ) were to present the impression for moment resistance along with eliminating the risk of a brittle collapsing (Carreira & Chu, 1985; El-Kholy et al., 2023; Emara et al., 2023; Hamoda et al., 2023b; Kim et al., 2024; Lin et al., 2022; Liu et al., 2020, 2023). This qualifies the designers to make decisions about the column's concrete type, cross-sectional area, and steel ratio.

2.2 Specified Details and Test Matrix

The reinforcement details used herein can be figured out in Fig. 1. In order to carefully evaluate the reflection of the four parameters, all columns were partitioned into four groups. The first group (G1) embraced three columns were specifically designated to explore the impact of the three concrete types (NC, ECC, and HSFRC). All columns of this group identically reinforced with 5D10 (giving $\mu = 2.2\%$) and 8 mm diameter each 200 mm (giving $\rho = 0.84\%$) as longitudinal reinforcement and stirrups, respectively, as shown in Fig. 1a, b and Table 1. The second group (G2) included four NC columns were designed to examine the effect of longitudinal reinforcement. Therefore, the four columns were longitudinally reinforced with 5D10, 4D10 + 2D8, 6D10 and 7D10 giving μ ratios of 2.20%, 2.30%, 2.60%, and 3.10%, respectively, while the stirrups were set as 8 mm diameter @ 200 mm as shown in Fig. 1a, c and Table 1.

For the third group (G3), the reinforcement ratio remained constant with 5D10 (i.e., $\mu = 2.2\%$), but the closed stirrup has been altered with ρ values of 0.84%, 0.93%, 1.00% and 1.18% as shown in Fig. 1a, d and Table 1. The last group (G4) studied the reflection of slenderness ratio through three identical NC columns had the same reinforcement details; however, the clearance height has been varied by moving the supports up-or-down giving λ ratios of 4.89, 4.51, and 4.14, as detailed in Table 1 and Fig. 1a, e. Both the longitudinal reinforcement ratio and stirrups amount were held constant as detailed in Table 1.

As can be seen in Table 1, all columns were labeled using a specific nomenclature: A-B-C-D. The first letter, A, represents the concrete kind which was: N,E or H for NC, ECC, or HSFRC, respectively. The second part, B, corresponds to the longitudinal reinforcement ratio employed, with choices of $\mu = 2.2\%$, 2.3%, 2.6%, or 3.1%. The third part, C, denotes the distance between the transverse steel stirrups, with possible values of 200, 181, 167, or 142 mm. Lastly, the fourth letter, D, if applicable, signifies the slenderness ratio of the tested column, which were $\lambda = L_1$ and L_2.

2.3 Material Properties and Mix Proportion

As it was mentioned above, the new generations of HPCs have been delivered herein through both ECC and HSFRC as an attempt to perfectly resist the unexpected additional cracks arising from edge moment. The higher strain-hardening fibrous concretes have been delivered

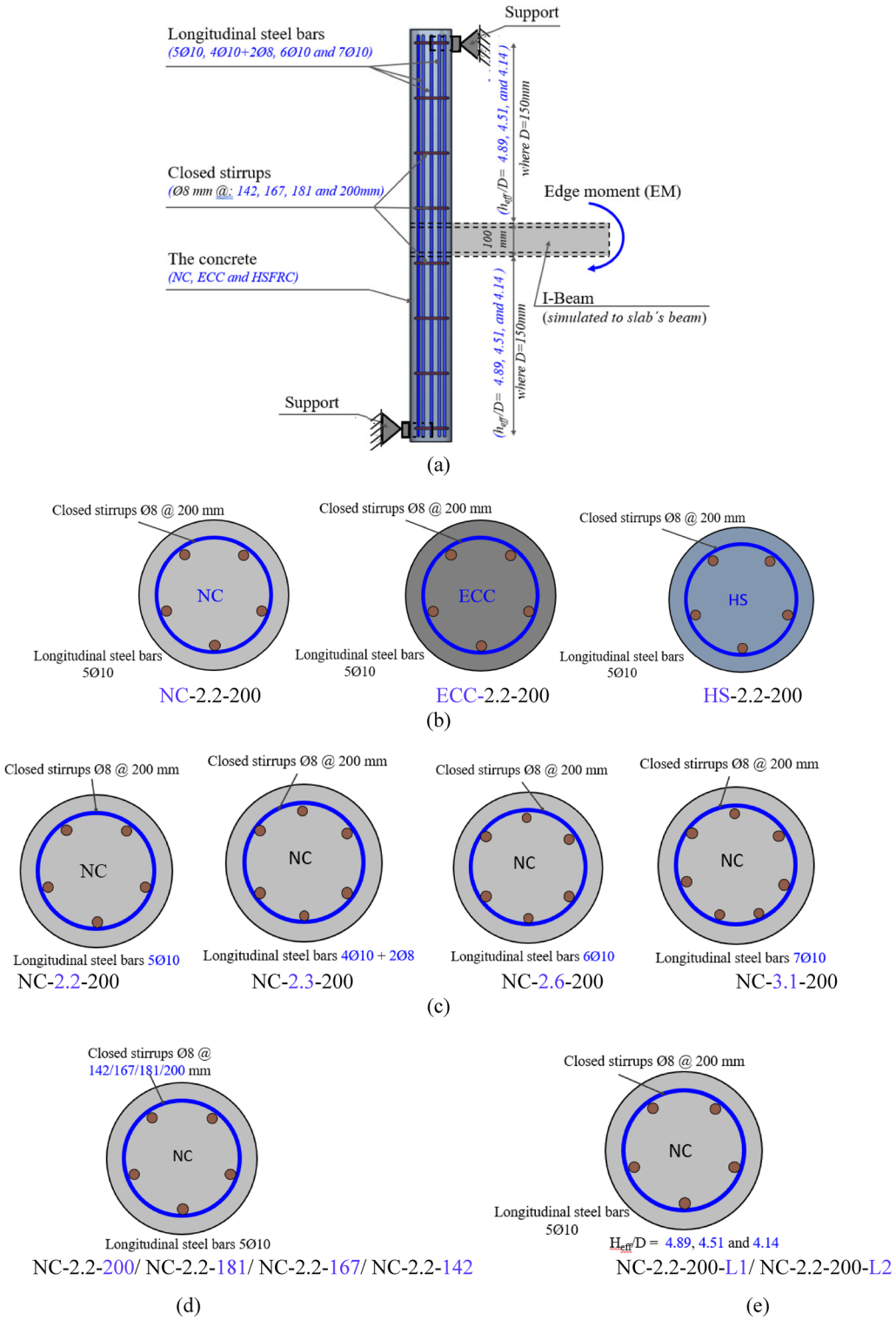

Fig. 1 Schematic details and variables of all the columns: **a** longitudinal details, **b** the first group, **c** the second group, **d** the third group; and **e** the fourth group

due to its better characteristics related to cracks controlling in terms of post- and pre-cracking. The concrete mixes have been considered herein as previously reported (Hamoda et al., 2019, 2021, 2023a, 2024a).

This investigation involved the use of three distinct types of concrete mixes: NC, ECC, and HSFRC as presented in Table 2. The first type, NC, represented a conventional mixture containing ordinary Portland cement,

Table 1 Test matrix and details of the tested columns

Group	Specimen's ID	Concrete	Longitudinal bars (μ %)**	Stirrups (ρ %)***	λ*	Studied parameter
G1	NC-2.2-200	*NC*	5D10 (2.20)	8@200 (0.84)	4.89	Concrete type
	ECC-2.2-200	*ECC*				
	HS-2.2-200	*HSFRC*				
G2	NC-2.2-200	NC	*5D10 (2.20)*	8@200 (0.84)	4.89	μ
	NC-2.3-200		*4D10 + 4D10 (2.30)*			
	NC-2.6-200		*6D10 (2.60)*			
	NC-3.1-200		*7D10 (3.10)*			
G3	NC-2.2-200	NC	5D10 (2.20)	*8@200 (0.84)*	4.89	ρ
	NC-2.2-181			*8@181 (0.93)*		
	NC-2.2-167			*8@167 (1.00)*		
	NC-2.2-142			*8@142 (1.18)*		
G4	NC-2.2-200	NC	5D10 (2.20)	8@200 (0.84)	*4.89*	λ
	NC-2.2-200-L1				*4.51*	
	NC-2.2-200-L2				*4.14*	

* λ is the effective clearance height-to-diameter ratio (H_e/D_c), **μ % is longitudinal reinforcement ratio (Abars/Ac) and ***ρ % is the stirrups to column ratio by volume (Vstirrup/Vspacing)

**μ % is ratio (A_{bars}/A_c)

***ρ % is the ratio by ($V_{stirrup}/V_{spacing}$)

Table 2 Mix proportion and concrete grade for different types

Concrete	Cement (kg/m^3)	F.Agg (kg/m^3)	C.Agg (kg/m^3)	F.A (kg/m^3)	W/b	PP (% in volume)	HRWR (kg/m^3)	f_c' (N/mm^2)	f_t (N/mm^2)
NC	355	698	1143	–	0.42	–	–	28	2.48
ECC	558	436	–	665	0.23	2.20	15	51	5.20
HSFRC	456	652	1098	26	0.29	2.00	9.5	79	7.12

Cement grade 52.50 N/mm^2, F.Agg.: fine aggregate, C.Agg.: coarse aggregate, F.A.: fly ash, W/b: water to bender ratio (bender = cement + F.A.), PP: polypropylene fiber, HRWR: high range water reducer

(a) (b) (c)

Fig. 2 Casting and preparation of RC columns: **a** reinforcement, **b** plastic molds confined with wooden forms, and **c** casting of the flowable ECC

natural siliceous sand and basalt coarse aggregate with weight ratios shown in Table 2. The second one was flowable ECC, as shown in Fig. 2, encompassed polypropylene (PP) fibers with 12 mm length, Portland cement, fly ash, and various admixtures as shown in Table 2. The last type was HSFRC high strength concrete comprising the same PP fiber used in ECC together with other components giving mix proportion can be seen in Table 2. The volume fraction has been specified by volume with percentage units in Table 2. The percentage of volume fractions were about 2.20% and 2.00% for both ECC and HSFRC, respectively, as previously reported (Hamoda et al., 2019, 2021, 2023a, 2024a). Both concrete mixes have been selected based on experienced studies which then gave approximately the concrete compression and tensile stresses (Hamoda & Hossain, 2019; Hamoda et al., 2023a, 2023b, 2024a).

The compressive strength of each concrete type was assessed by calculating the average value from three standard cylindrical specimens, measuring 150 mm in diameter and 300 mm in height. As a result, the average compressive strengths were determined to be 29, 51, and 79 N/mm^2 for NC, ECC, and HSFRC, respectively. The Egyptian code practice classifies the high strength concrete starting from 65 MPa (El-Shennawy et al., 2013). Fig. 3a provides the geometric details for typical test samples recommended to US requirements (Committee, 2008) with doubling the sizes. Tensile tests were conducted on dog-bone specimens with universal test machine giving the adequate mode of failure shown in Fig. 3. The average tensile strength values obtained from these tests were about 2.48, 5.20 and 7.12 N/mm^2 for NC, ECC and HSFRC, respectively.

Two types of steel bars were utilized herein for all the columns. High-strength deformed steel bars with 10 mm diameter and normal-strength smooth 8 mm diameter agreed with grade of 351/532 and 291/445, respectively, were delivered for longitudinal and lateral reinforcement. The modulus of elasticity for the 10 mm diameter steel bars was approximately 197 GPa, while the 8 mm diameter plain bar was about 189 GPa. The stress–strain relationships of such bars are shown in Fig. 4, while the specific details are summarized in Table 3. These findings provided valuable insights into the mechanical properties to better justify and analyze the test results in addition to constructing the FEMs.

2.4 Test Set-Up and Instrumentation

All columns were set up with limited movement at both the top and bottom ends as the constant boundary conditions shown in Figs. 1a and 5. Then, to simulate the rotational edge moment, demountable strong steel I-beam welded with half cylindrical steel tube confining the column's surface with the other half through bolts as detailed in Fig. 5 (demountable steel I-beam). The steel I-beam was primarily set to generate the required edge moment. To achieve that; at the I-beam's free end, an increasing jacking load was positioned at 1.00 m length from column's axis to deliver constant edge moment simulating to that of the floor's beam. Moreover, for this simulation to appear correctly, the I-beam's free end was allowed for rotation during the loading by attaching real hinge joint at the upper I-beam's flange shown in Fig. 5

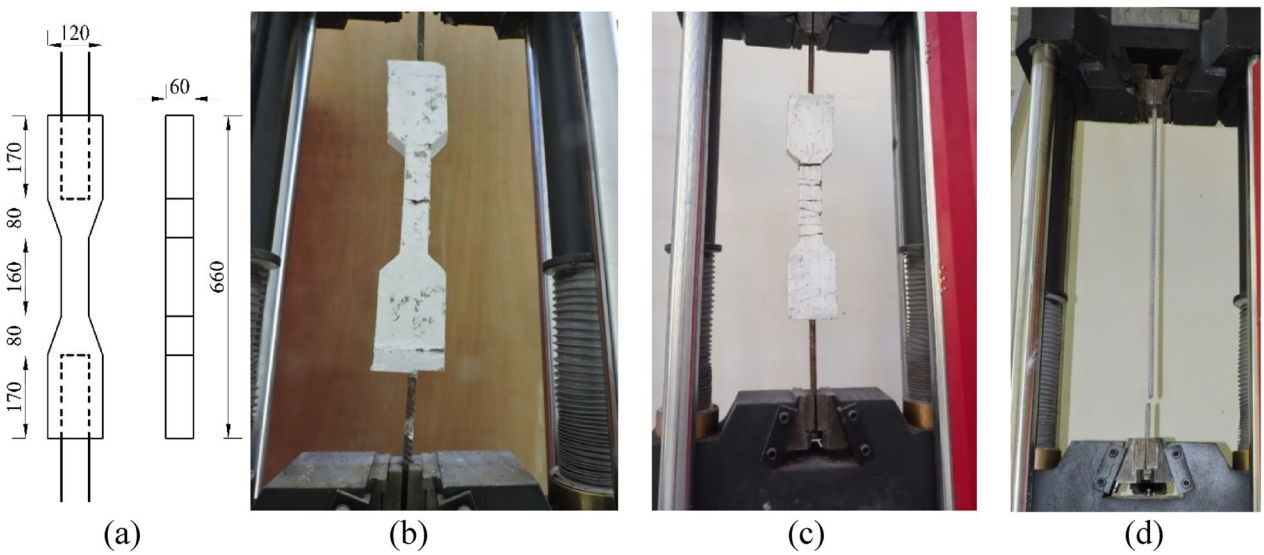

Fig. 3 Uniaxial tensile tests: **a** dimension of the tensile dog-bone test, **b** normal concrete, **c** engineered cementitious composite, and **d** steel bars

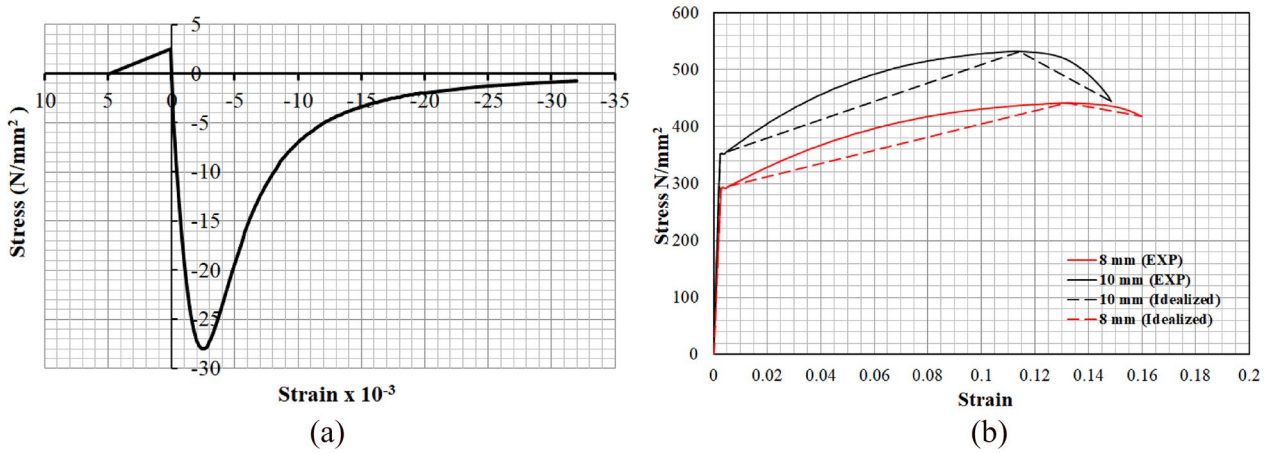

Fig. 4 Stress–strain curves calibrated based on experimental tests. **a** NC adapted with Carrier and Chu (1985) and **b** steel bars

Table 3 Material properties of reinforcing steel

Diameter	Yield stage		Ultimate stage		Failure stage		*E* (GPa)	Poisson's ratio
	σ_y (MPa)	ε_y (%)	σ_u (MPa)	ε_u (%)	σ_f (MPa)	ε_f (%)		
8 mm	291	0.156	445	13.21	423	16.01	189	0.30
10 mm	351	0.178	532	12.32	453	15.51	197	0.30

σ: stress; ε: strain; E: modulus of elasticity

(hinge joint). The instrumentation has been proposed and installed to simply record the first visual crack, of based on it recording the cracking width (by PI-gauge), displacement (by LVDT) and the load value (by attached load cell). Also, the same procedures have been respected for reading that data of both yield and ultimate stage. To measure rotational angle, linear variable differential transducer (LVDT) was positioned at the loading point which is about 1.00 m length from the column axis. Also, two steel strain gauges were attached on the tensile and compression longitudinal steel bars to approximately estimate the tensile and compressive strains. In addition, two PI gauges have been mounted on the compression and tension column's surfaces as shown in Fig. 5 (PI-gauge details). Throughout the testing procedure, various sensitive results were recorded for each specimen, including the load–rotation relationship, the cracking moment, ultimate and failure load, and steel strain relationships. The load was supplied with an increment of about 5 kN increment and the cracks were recorded and leveled during the test. Such load increment was suitable for the used hydraulic jack to be controlled and also was previously reported and performed in some studies extracted from the same lab (Committee, 2008; Hamoda et al., 2023a, 2023b, 2024a, 2024b).

3 Test Results and Discussion

The failure modes, cracking features, ultimate-carrying capacity, moment–rotation responses, elastic stiffness and energy dissipation capacity for the experimented columns are analyzed in this section. Table 4 summarizes the test outcomes regarding the loads recognized at cracking and ultimate zones (P_{cr} and P_u, respectively), together with their corresponding rotation values (θ_{cr} and θ_u, respectively). A brief chart comparing the recorded moments at cracking, yield and ultimate stages in addition to the absorbed energy can be seen in Fig. 12. The crack patterns and collapse mode for all experimented columns are shown in Figs. 6, 7, 8, 9 and 10.

3.1 Crack Pattern and Failure Mode

Generally, the RC circular columns exposed to excessive rotational edge moment could form two major reversed damaged zones. One of them is affected by compression stresses, while the other counterpart is captured tensile cracking stresses. The tensile cracked zone may be described as an elongated half-oval shaped formed just at the edge of the beam–column joint where tensile stresses can exist with peaked values. On the other side, the compression rival can be identified by concrete crushing with deterioration feature starting just at the edge of the beam–column joint.

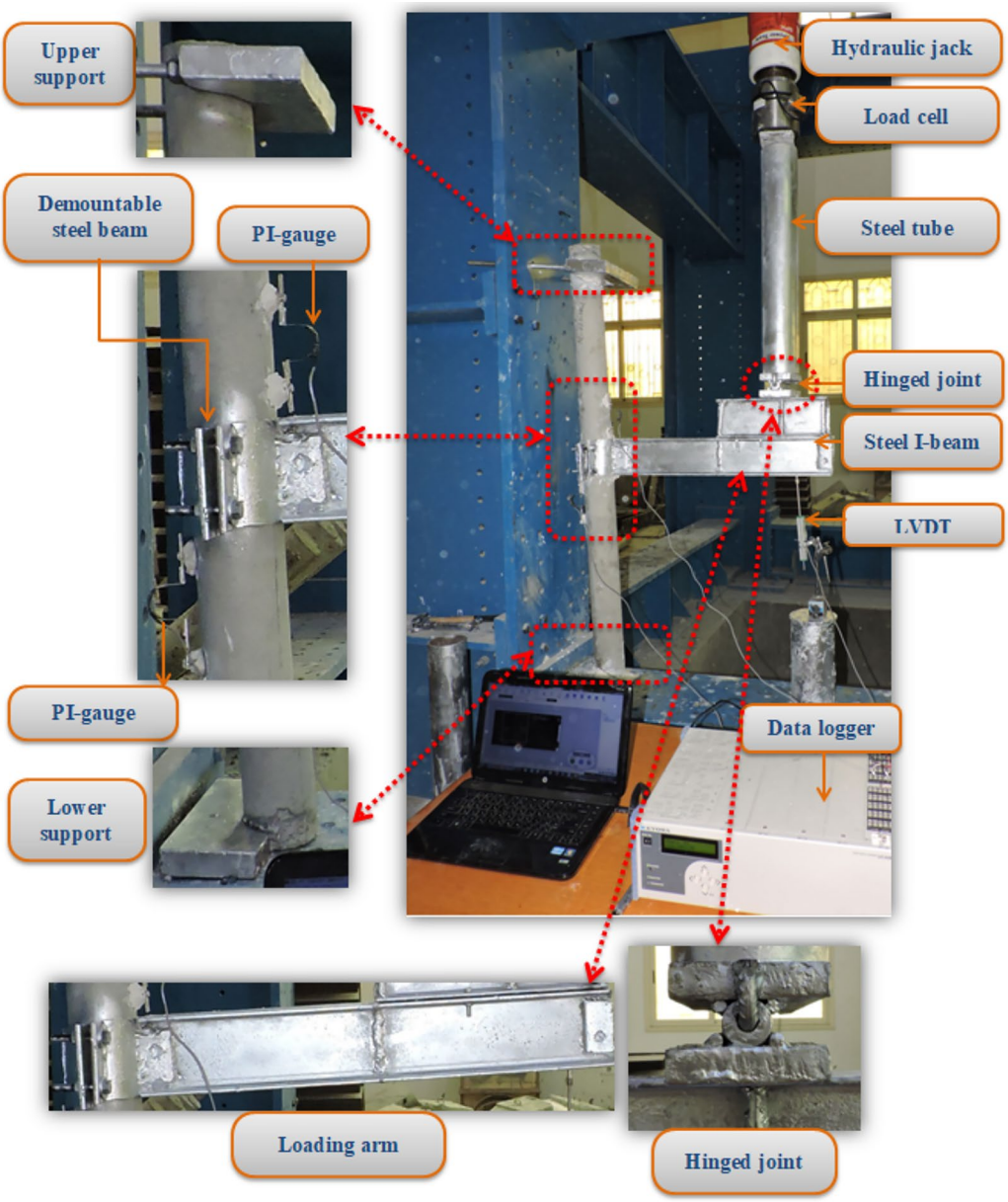

Fig. 5 Experimental picture of test set-up and instrumentation

The master column (NC-2.2-200), presented the first hairline cylindrical tensile crack with half-oval form at a moment of 7.42 kN m (about 24% of M_u) as shown in Table 4. Then, related to the tension zone, the significant crack opening gradually widened accompanied with small cracks appeared with higher elongated half-oval shape. Just before failure, cracks formed at tension side become with more elongated half-oval shape with wider opening followed by sudden concrete crushing just at the edge of beam's joint and, consequently, column collapse as shown in Fig. 6. The current column could not sustain about $M_u = 24.46$ kN m leading to failure.

Columns made of ECC and HSFRC displayed crack pattern that can be identified in Fig. 7. Initially, very few hairline cracks slightly appeared with half-oval shaped at the tension zones referring to the mechanism of load transferring into the tested column. However, both ECC and HSFRC types presented controllable cracking width than that of NC column. It was noted that the first tensile crack width observed by the ECC column was more tightened than that of the HSFRC counterpart. Then,

Table 4 Test outcomes

Group	Specimen's ID	Cracking Stage				Yield stage			Ultimate stage			*(ES)		**(E)		***
		M_{cr} (kNm)	M_{cr}/M_{cr0}	θ_{cr} (°)*10^{-3}	W_{cr} (mm)	M_y (kNm)	M_y/M_{y0}	θ_y (°)*10^{-3}	M_u (kNm)	M_u/M_{u0}	θ_u (°)*10^{-3}	K	K_B/K_{B0}	E	E/E_0	Failure mode
G1	NC-2.2-200	7.42	1.00	4.14	0.24	24.46	1.00	9.63	30.58	1.00	15.77	3.25	1.00	304	1.00	C
	ECC-2.2-200	10.38	1.40	5.62	0.09	30.38	1.24	11.52	36.46	1.19	17.64	3.93	1.21	408	1.34	
	HS-2.2-200	11.45	1.54	5.81	0.15	31.45	1.29	12.13	38.39	1.26	17.14	4.37	1.34	407	1.34	
G2	NC-2.2-200	7.42	1.00	2.28	0.24	24.46	1.00	9.63	30.58	1.00	15.77	3.25	1.00	304	1.00	C
	NC-2.3-200	8.25	1.11	2.16	0.23	32.08	1.31	10.21	39.12	1.28	16.57	3.82	1.18	422	1.39	F + C
	NC-2.6-200	8.16	1.10	2.10	0.23	38.66	1.58	10.37	45.47	1.49	16.86	3.89	1.20	516	1.70	
	NC-3.1-200	9.93	1.34	2.61	0.21	42.64	1.74	11.39	46.32	1.51	16.95	3.8	1.17	529	1.74	
G3	NC-2.2-200	7.42	1.00	2.28	0.24	24.46	1.00	9.63	30.58	1.00	15.77	3.25	1.00	304	1.00	C
	NC-2.2-181	7.96	1.07	2.00	0.24	28.69	1.17	11.89	30.83	1.01	15.50	3.98	1.22	309	1.02	F + C
	NC-2.2-167	9.07	1.22	2.35	0.24	30.31	1.24	11.03	35.06	1.15	15.32	3.75	1.15	334	1.10	
	NC-2.2-142	9.25	1.25	2.26	0.24	32.68	1.34	10.84	38.57	1.26	17.22	4.09	1.26	428	1.41	
G4	NC-2.2-200	7.42	1.00	2.28	0.24	24.46	1.00	9.63	30.58	1.00	15.77	3.25	1.00	304	1.00	C
	NC-2.2-200-L1	8.50	1.15	2.13	0.24	31.75	1.30	9.29	40.66	1.33	14.60	3.99	1.23	366	1.20	
	NC-2.2-200-L2	9.57	1.29	2.10	0.23	36.27	1.48	8.30	50.07	1.64	15.16	4.53	1.39	476	1.56	

*(ES): elastic stiffness

**(E): absorbed energy

***Failure mode: C = compression failure signed by concrete crushing; F + C = flexural deterioration followed by compression failure

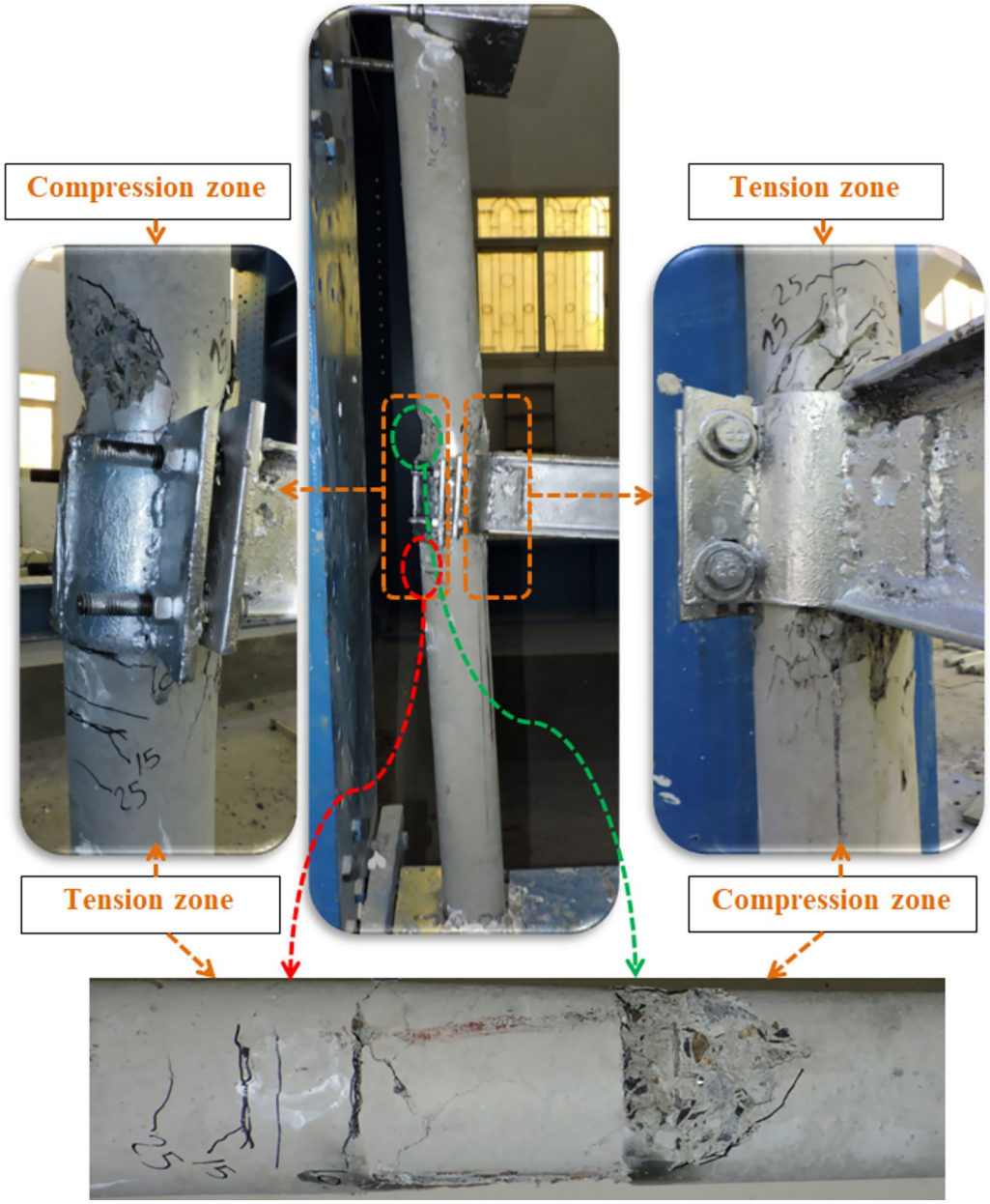

Fig. 6 Typical crack pattern of RC circular columns subjected to EM (master column NC-2.2-200)

as the load was increased, several cylindrical-half-oval cracks have been increased parallel to the major one. Moreover, it was column ECC-2.2-200 that showed several random cracks with smaller widths compared to that of HS-2.2-200. Just before failure, sudden concrete crushing was detected at the two sides opposite to the tension ones recording an ultimate load of 36 and 38 kN m for columns ECC-2.2-200 and HS-2.2-200, respectively. All columns behaved flexural cracks followed by compression failure mode evidenced by concrete crushing as shown in Fig. 7.

For the second group, at which the parameter of longitudinal steel bars ratio was explored, Fig. 8 presents the crack pattern and failure mode. The first crack has been formed encircling the column section at the tension side appeared at a moment of 8.25, 8.16 and 9.93 kN m (estimated within range of 17%–21% of M_u) for columns NC-2.3-200, NC-2.6-200 and NC-3.1-200, respectively. Also, the initial moment level has been increased with

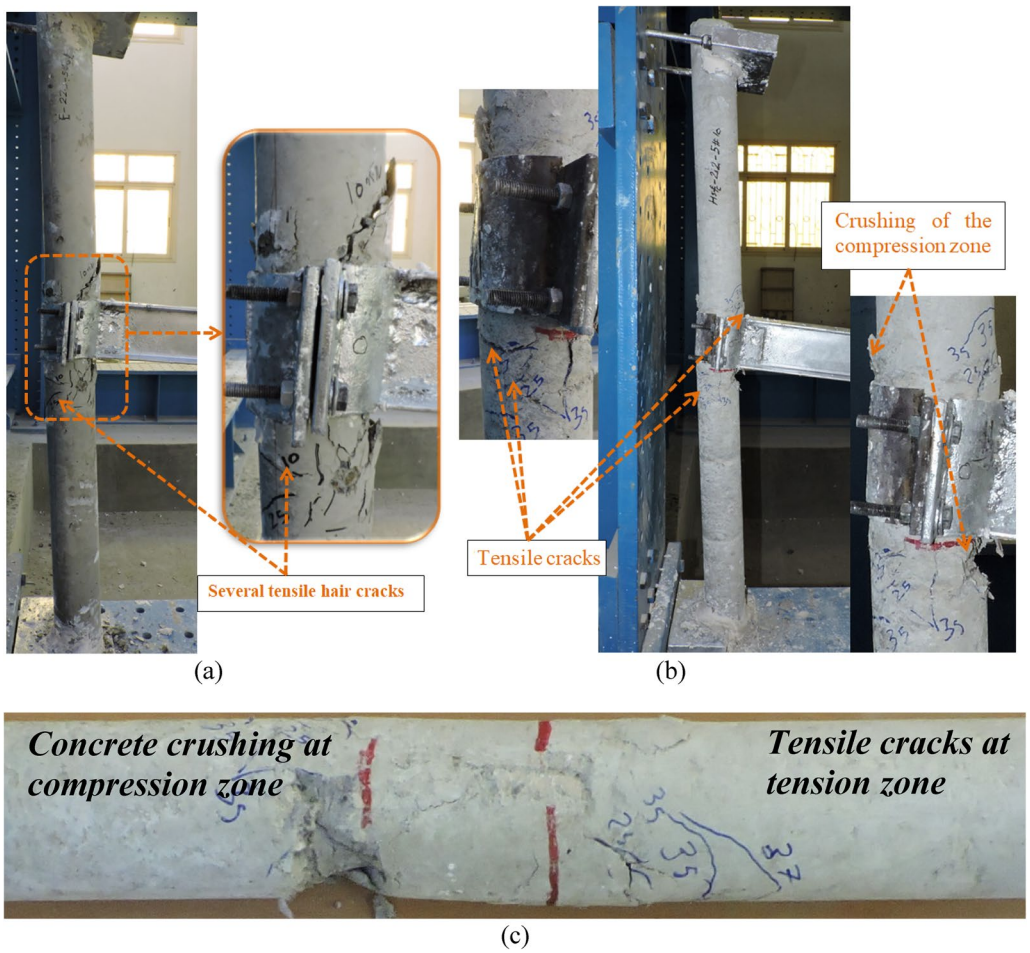

Fig. 7 Typical crack pattern group G1: **a** ECC-2.2-200; and **b** HS-2.2-200; **c** mode of tension and compression deterioration

the increase of longitudinal steel ratio. At each given load, several cracks have been drawn with half-oval shaped at the tension sides; however, the distance of these cracks seemed to have lower spacing close to the beam–column joint. Just before failure, the region of tension cracks became enlarger and started to be dislocated near the connection zone. Also, it is worth mentioning that the columns had higher μ ratio tended to behave the flexural with-or-without compression failure mode with propagated cracks followed by detachment of the half-oval tension part. Columns could not sustain any jacking load presenting flexural failure mode for columns NC-2.3-200 and NC-2.6-200 as shown in Fig. 8a, b, respectively. Besides, column with higher ratio (i.e., NC-3.1-200 with 3.1%) showed flexural failure associated with sudden concrete crushing at compression zone as shown in Fig. 8c.

Crack pattern and failure mode for group G3, where the effect of lateral reinforcement ratio ρ was studied can be seen in Fig. 9. At the beginning, small hairline cracks slightly grew with half-oval form at the tension regions with loads of 7.96, 9.07 and 9.25 kN m (estimated within range of 23%–25% of M_u) for columns NC-2.2-181, NC-2.2-167 and NC-2.2-142, respectively. This can reflect that the higher stirrups volume ratio results in the higher P_{cr} value as evidenced by column NC-2.2-142 with about 33% increase compared to the master one. As the jacking load was increased, the formation of cracking map has been enlarged in particular with those columns having smaller ρ as manifested by columns NC-2.2-181. Just before failure, the tensile cracking zone seemed to be dislocated with small conjunction cracks as shown in Fig. 9a, b for columns NC-2.2-181, NC-2.2-167, respectively. However, all columns almost exhibited sudden concrete crushing just at the edge of the cylindrical steel tube leading to failure achieving an ultimate load of about 30.83, 35.06 and 38.57 kN m for columns NC-2.2-181, NC-2.2-167 and NC-2.2-142, respectively. Concrete crushing in conjunction with dislocation of the elongated half-oval shape formed at the tension zone can be labeled as the mode of failure as shown in Fig. 9.

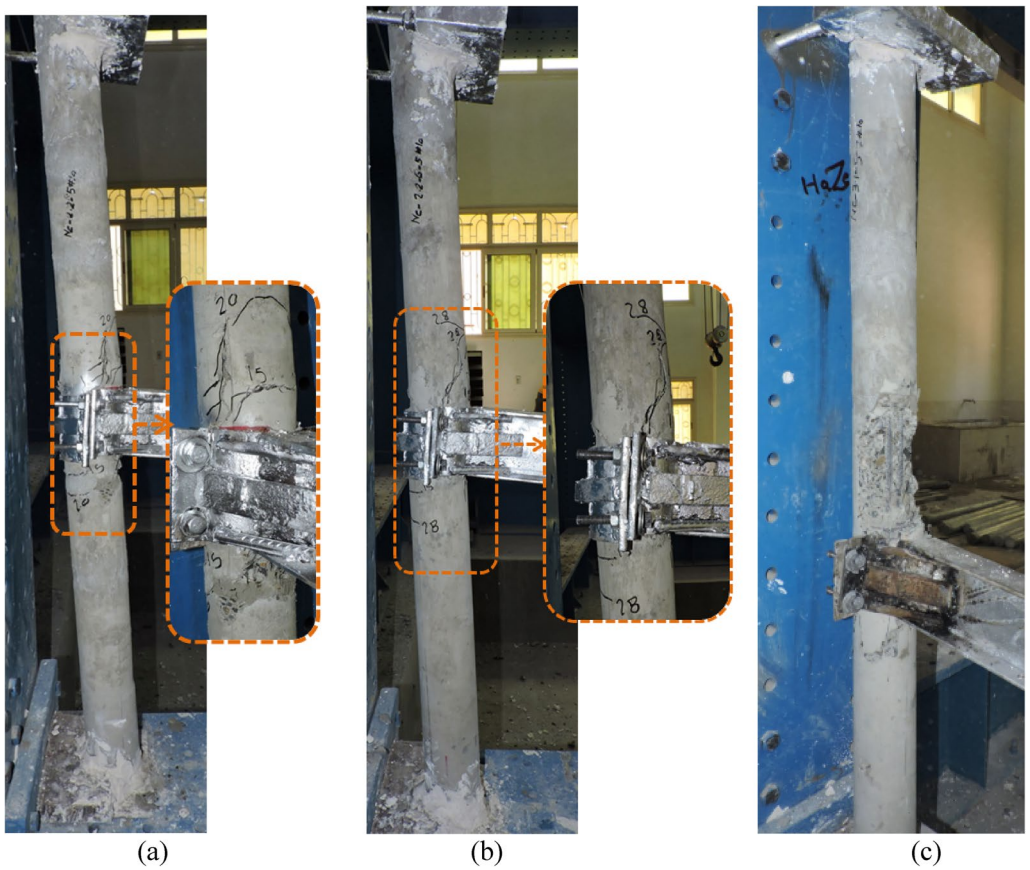

Fig. 8 Typical crack pattern group G2: **a** NC-2.3-200; **b** NC-2.6-200 and **c** NC-3.1-200

The impact of H_e/D_c slenderness ratio of RC circular columns subjected to double curvature moment as experimented in the fourth group G4 appeared with crack pattern shown in Fig. 10. Parallel to those tested earlier, the first crack formed at the tension zone encircling the half column surface at moments of 8.50 kN m and 9.57 (about 26%–26% of M_u), respectively, for columns NC-2.2-200-L1 and NC-2.2-200-L2 as shown in Table 4. Then, the two specimens started to produce more tensile cracks; however, column with larger slenderness ratio displayed larger tension cracks as shown in Fig. 10b for column NC-2.2-200-L2. Just before failure, the tensile cracked zone showed a dislocation of an elongated half-oval shape just at the edge of the beam–column joint at peaked load values presented an ultimate moment of 40.66 and 50.07 kN m for columns NC-2.2-200-L1 and NC-2.2-200-L2, respectively. However, and as it was expected to be, the column with larger H-to-D ratio appeared with more deformability bringing the double buckling shape along the column axis as shown in Fig. 10b for column NC-2.2-200-L2.

3.2 Moment–Rotation Response and Elastic Stiffness

Fig. 11 presents moment–rotation response for the all tested columns measured up to failure. Table 4 supplies the rotational angle value of all the columns obtained at cracking, yield and ultimate moment values.

Generally, the behavior of moment-rotational response can be partitioned into three zones, those may be: elastic, elastic–plastic with hardening feature, and softening performance up to failure. The elastic stage represents the non-cracked performance initiating from zero moment until the first cracking moment. Contextually, all columns performed approximate elastically up to the appearance of the first cracking which can be impressed with almost smaller values as manifested in Table 4. Beyond that, all specimens seemed to present an elastic–plastic response with an obvious hardening up to the peak. Finally, softening exhibition up to failure was characterized for all columns.

The moment–rotation response for columns made of HPCs can be seen in Fig. 11a for the first group G1. The moment–rotation response of HSFRC and ECC columns

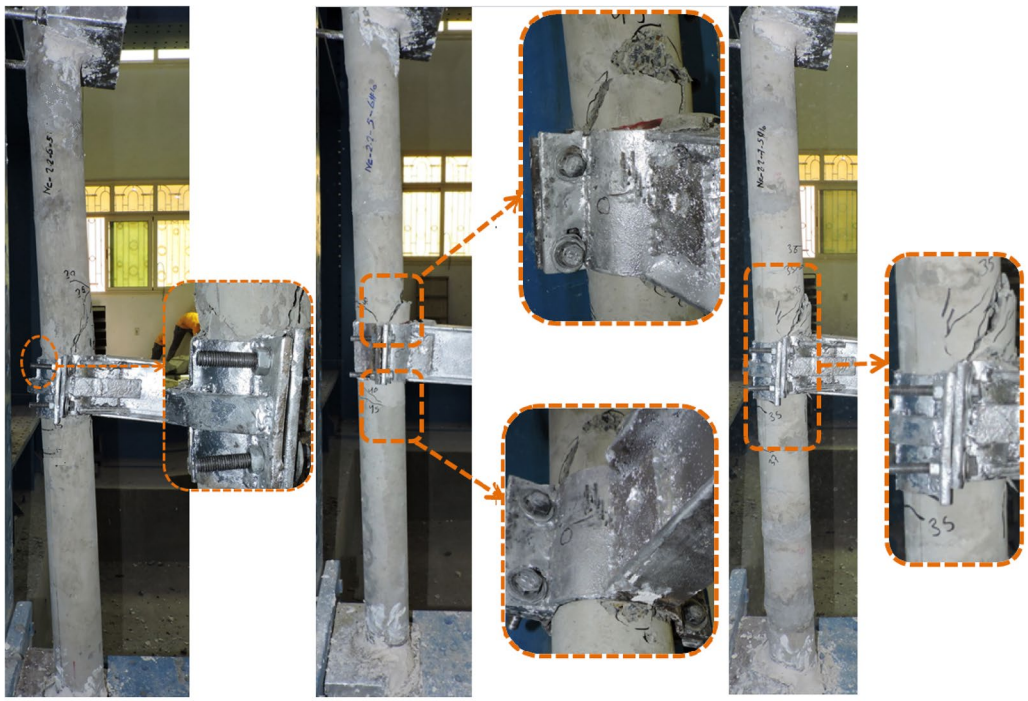

Fig. 9 Crack pattern and failure mode G3 specimens: **a** NC-2.2-181; **b** NC-2.2-167, and **c** NC-2.2-142

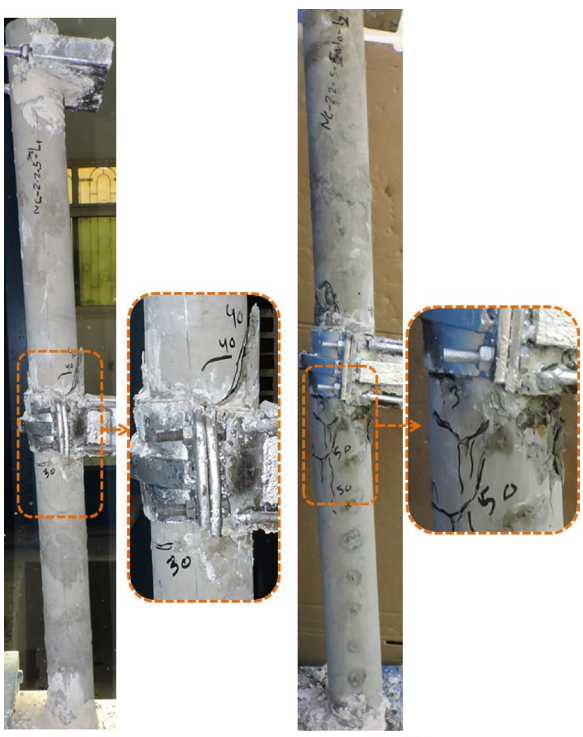

Fig. 10 Crack pattern and failure mode for group G4: **a** NC-2.2-200-L1 and **b** NC-2.2-200-L2

was significantly enhanced contrasting to that of the NC one which may be attributed to the hardening exhibition of fibered HPCs. The better contribution of HPCs has been reflected in elastic stiffness as manifested for columns made of ECC and HSFRC which have been increased by about 20% and 34%, respectively, compared to the ordinary column.

The effect of longitudinal reinforcement ratio exploited in the second group G2 can be appeared with moment–rotation response shown in Fig. 11b. All columns have been displayed with approximately the similar path exhibited by the master column except remarkable increase in the load level values with the increase of steel ratio. Such increase was recorded effectively for μ ratio ranged in between 2.6% and 3.1% presenting the same trend of upgrading. Moreover, it was emphasized that the contribution of longitudinal reinforcement augmented elastic stiffness within range of 16%–19% compared to the ordinary NC counterpart.

Test results confirmed that the parameters: height-to-diameter ratio together with longitudinal reinforcement could significantly affect and control the elastic stiffness. However, such enhancement could be upgraded to 40% with the presence of longitudinal reinforcement ratio with 3.10%. Thus making the studied parameters are

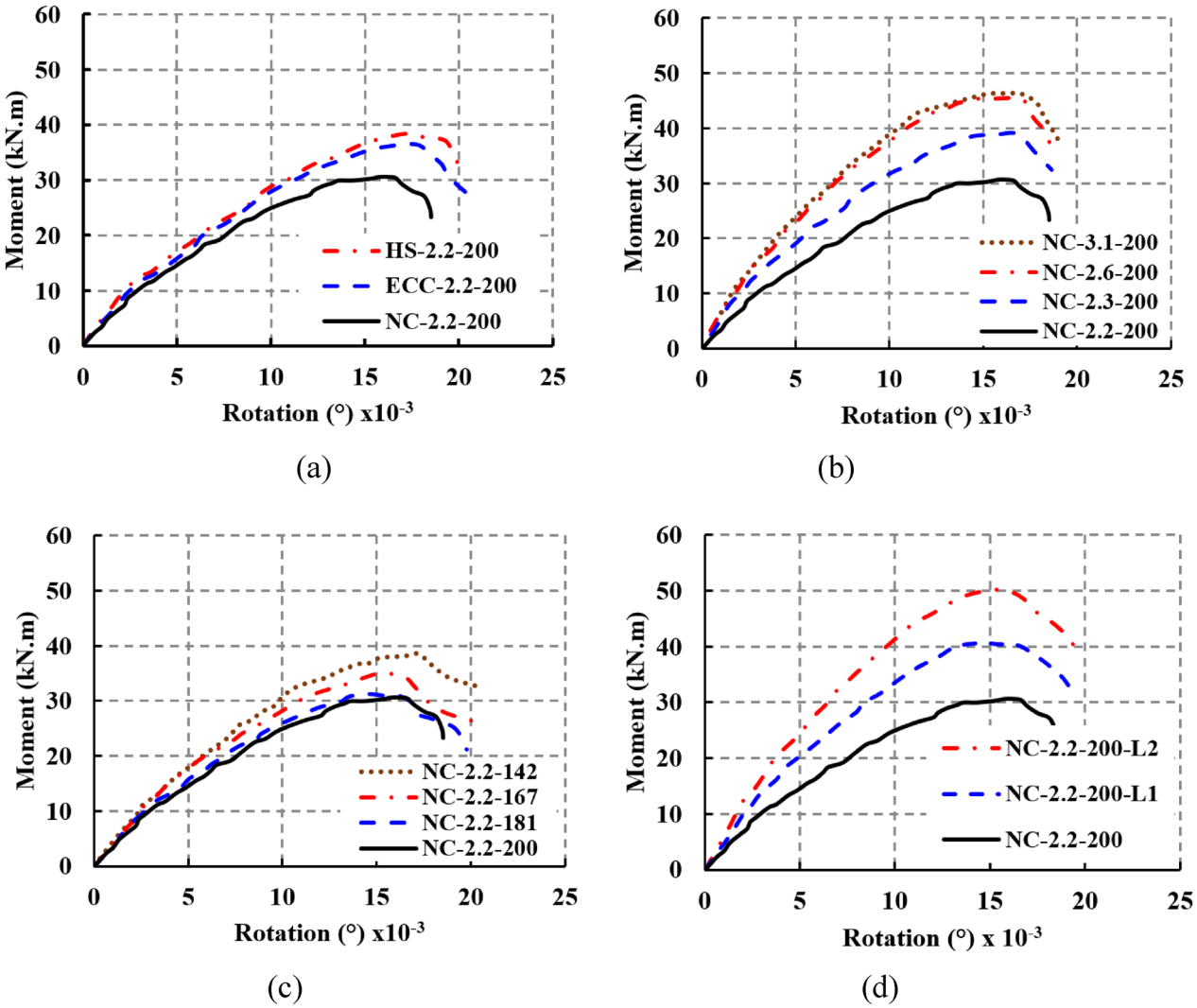

Fig. 11 Moment–rotation response for all groups: **a** Group G1, **b** Group G2, **c** Group G3, and **d** Group G4

very important for designers in case of sudden and unexpected overloading.

The existence of lateral reinforcement experimented in group G3 appeared with moment-rotational response can be seen in Fig. 11c. The lateral reinforcement ratio of $\rho = 0.93\%$ for column NC-2.2-181 showed very close performance to that of the master column. However, increasing stirrups ratio to 1% and 1.18% presented an upgraded moment–rotation response compared to control column as evidenced in columns NC-2.2-167 and NC-2.2-142, respectively, as shown in Fig. 11c. Also, it can be mentioned that the hardening feature has been improved by increasing this ratio as shown in Fig. 11c. All columns in this group enhanced the elastic stiffness compared to the master one within range of (15%–25%). However, the higher stirrups ratio which is 1.18% upgrade the elastic stiffness by about 25% as evidenced by column NC-3.1-200 as shown in Table 4. This may be attributed to the considerable confinement achieved by the closed stirrups along the column length leading to augment the concrete core of the circular column.

The height-to-diameter ratio has been presented in the fourth group in term of moment–rotation response shown in Fig. 11d. As shown in Table 4, comparing the all rotation angle values revealed that the smaller height-to-diameter ratios presented the smaller deformation feature as it was expected. Comparing the studied variables has been reflected in the deformation shape. Table 4 emphasizes that the degree of rotational angle recorded at cracking, yield and ultimate stages were found to be diminished by about 7% and 8%, 4% and 14%, beside 8% and 4%, respectively, each for columns NC-2.2-200-L1 and NC-2.2-200-L2, respectively. Moreover, this can be confirmed by upgrading observed by elastic stiffness that

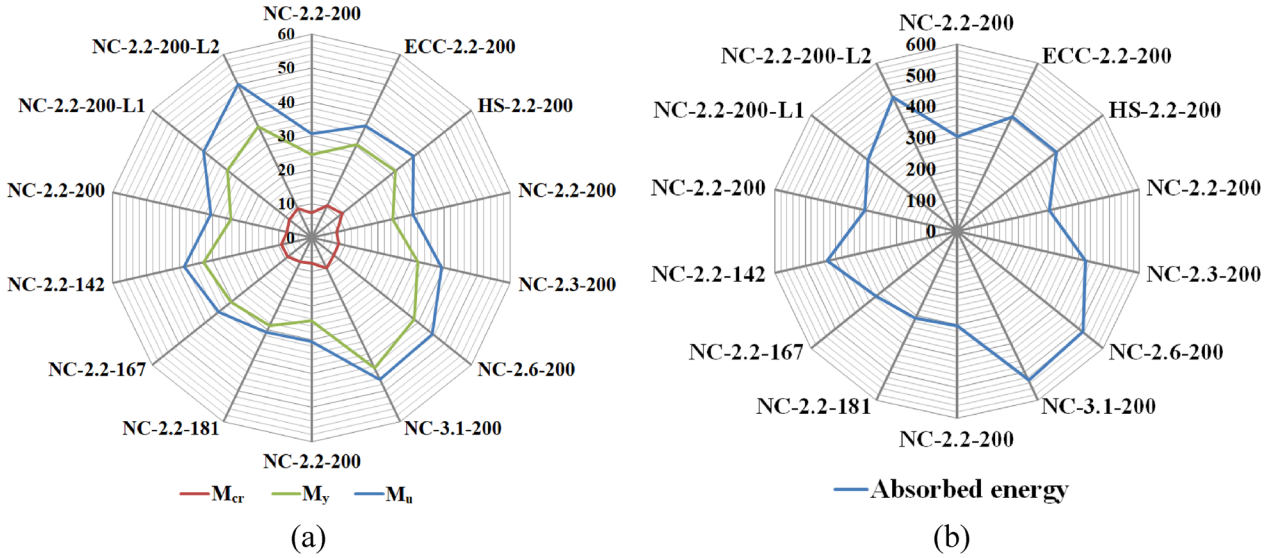

Fig. 12 Chart of test results: **a** moment measured at the three stages and **b** absorbed energy

has been enhanced by about 22% and 40% for columns NC-2.2-200-L1 and NC-2.2-200-L2, respectively.

3.3 Ultimate Capacity

Table 4 provides the ultimate load achieved by all the columns during the experimentation. The presence of ECC and HSFRC could increase the ultimate load-carrying capacities by about 19% and 25%, respectively, as shown in Fig. 12a. However, it is worth mentioning that for columns having the identical geometric properties and slenderness ratio, the factor of longitudinal steel bar appeared with very considerable contribution to the ultimate capacity compared to other counterparts. The effect of using longitudinal reinforcement with ratios of: 2.30%, 2.60% and 3.10%, upgraded the load-carrying capacity by about 27%, 48% and 51%, respectively, compared to the control one with 2.20% as shown in Fig. 12a. This may be expected to be since it is very considerable factor could directly resist the lateral moment as previously reported (Alajarmeh et al., 2020; Aules et al., 2020; Barua et al., 2021). On the contrary, the parameter of closed stirrups appeared with the lower reflection since the maximum detected upgrading was about 25% as shown in Table 4. Owing to the fact that the He/Dc ratio was dropping, the impact tended to be limited. H_e/D_c Therefore, the use of λ ratio with about 4.51 and 4.14 led to increasing the ultimate load by about 33% and 63%, respectively. The parameter of slenderness ratio could significantly control the buckling moment resistance responsible for column's moment carrying capacity. Therefore, the buckling moment and consequently the double curvature buckling deformation could be decreased with the increase of slenderness ratio (Afefy & El-Tony, 2016). This has been manifested herein experimentally as shown in moment–rotation response shown in Figs. 11d and 12.

3.4 Absorbed energy

Table 4 and Fig. 12b display the absorbed energy (E) of each tested column which is evaluated as the area under the moment–rotation curve. The use of fibrous concrete increased the absorbed energy by about 33% and 34% as recorded by columns ECC-2.2-200 and HS-2.2-200 made of ECC and HSFRC, respectively. Such enhancement was also previously reported (Hamoda et al., 2023a, 2023b) due to the better reflection of strain hardening ECC characterized by and tightened effect and bridging action as a results of PP fiber existed in HSFRC. However, the significant enhancement was credited to the parameter of longitudinal reinforcement ratio. This may be expected to be since it is the main factor resisting the lateral moment with direct action as in previous studies (Kim et al., 2024; Li et al., 2023; Lin et al., 2022). Results showed that longitudinal steel ratios of $\mu = 2.30\%$, 2.60% and 3.10% gave rise to significantly augmented absorbed energy by about 39%, 70% and 74%, respectively (as observed from columns: NC-2.3-200, NC-2.6-200 and NC-3.1-200, respectively). Although the closed stirrups gained only about 10% contribution, it was the lower improved energy detected compared to other factors as was expected. This may be attributed to its lateral position which prevented the direct contribution for resisting the lateral moment as previously reported (Hou et al., 2023; Zhou et al., 2023). The factor of closed stirrups could be considered with the higher ratio equalled to $\rho = 1.18\%$ as

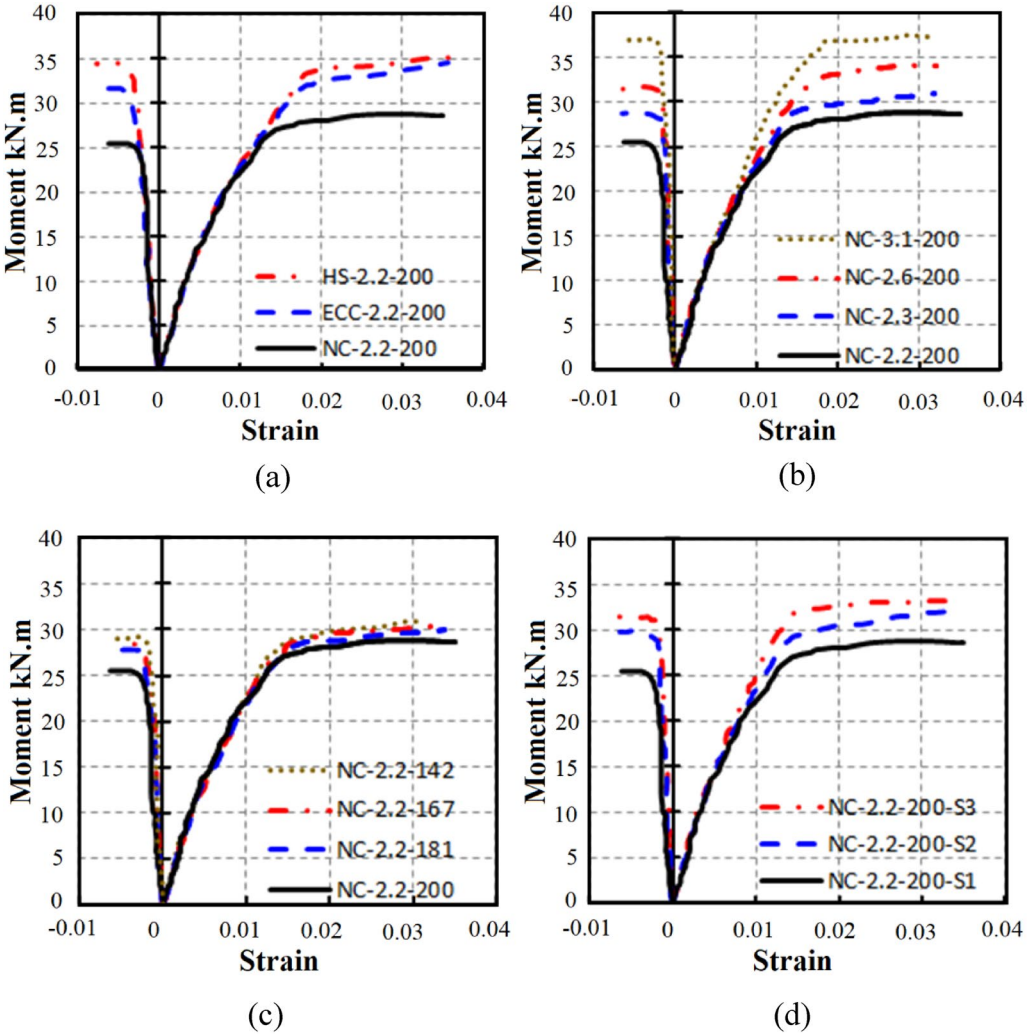

Fig. 13 Moment–strain response: **a** Group G1; **b** Group G2; **c** Group G3; and **d** Group G4

obtained experimentally by column NC-2.2-142 which enlarged the E value by about 40%. The fourth group detected that the lower H_e/D_c ratios with values of 4.51 and 4.14 could increase the absorbed energy by about 20% and 56% as observed by columns NC-2.2-200-L1 and NC-2.2-200-L2. Fig. 11d emphasizes that the lower H_e/D_c ratio increased the absorbed energy which may be attributed to the higher resistance moment. This was expected owing to increasing moment values and consequently increasing the absorbed energy calculated from moment–rotation response (Fig. 13).

4 Numerical Simulation

A numerical simulation was conducted to analyze the behavior of RC circular columns examined experimentally. To accomplish this, a nonlinear three-dimensional (3D) finite element model (FEM) was constructed utilizing finite element software program. The model was carefully established against experimental outcomes to gain its accuracy and reliability.

4.1 Model Built-Up, Interaction Properties, and Boundary Conditions

In the current study, the tested columns were modeled considering the geometrical details and material properties. To achieve this, eight-node linear reduced integration solid elements (C3D8R) were delivered to accurately model the concrete types the loading parts.

In order to define the behavior of the longitudinal and lateral reinforcement, two-node linear 3D truss elements (T3D2) were utilized, as illustrated in Fig. 14. The load was precisely applied to a reference point that was

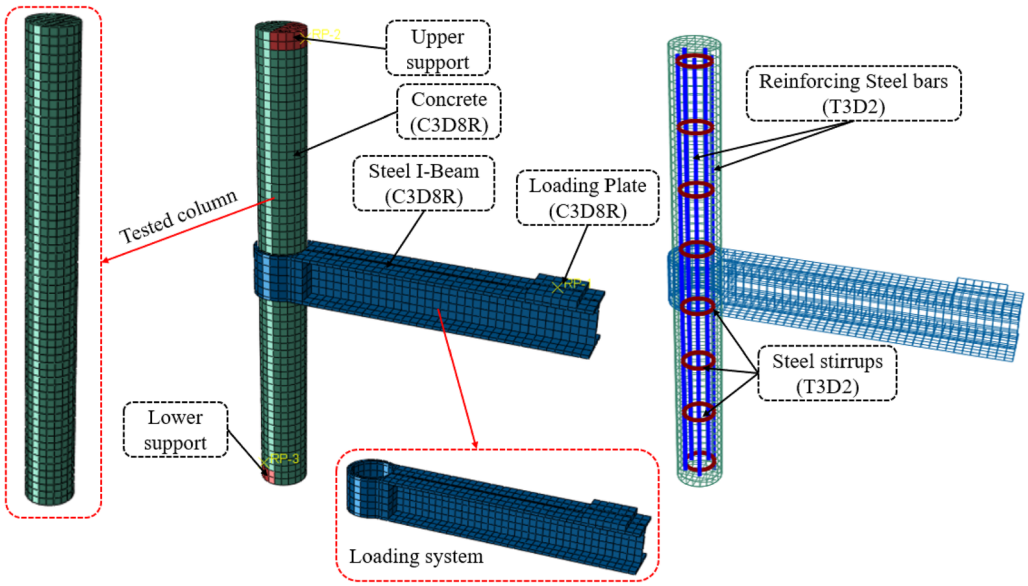

Fig. 14 3D finite element model set-up

securely connected to a rigid loading plate, as shown in Fig. 14. With respect to the experimental set-up, the numerical simulation aimed to deliver dependable and precise results regarding the behavior of the investigated RC columns. This approach ensured a high level of reliability and accuracy in the study's findings.

The interaction between reinforcing steel bars (i.e., longitudinal bars and stirrups) and the concrete was delivered numerically through the embedded region constraint. In such modeling criteria, the concrete was set as the host region, while the reinforcements were considered as the embedded elements (Hamoda & Hossain, 2019; Hamoda et al., 2019, 2021, 2023a, 2024a). Modeling of steel bars and stirrups as embedded elements permitted the realistic representation of the bond behavior between the steel reinforcement and the surrounding concrete. Then the partition I-beam loading arm was assembled together with the concrete column identically to the experimental situation as shown in Fig. 14.

4.2 Constitutive Modeling of Materials

The Concrete Damage Plasticity (CDP) model was selected to model the concrete element. This model is well-suited for simulating both the compressive and tensile behaviors of concrete mechanical properties. In similar context, CDP has better ability for exemplifying the deterioration arising from concrete cracking and nonlinear deformations in compression and tension with respect to damaged nonlinearity algorithm. Moreover, it employs the principle of isotropic damage elasticity together with isotropic compression and tension nonlinearity to model the plastic performance of concrete under tensile and compressive stresses (Afefy & El-Tony, 2016; Liu et al., 2020; Mostafa, 2024). For the simulation of NC, Eqs. 1 and 2 proposed by Carreira and Chu (Carreira & Chu, 1985) were delivered for plotting the compressive stress–strain response, shown in Fig. 4a, with respect to the experimental outcomes explained in Sect. 2.3:

$$\sigma_c = f_c \left[\frac{\beta \left(\frac{\varepsilon_c}{\varepsilon_{c0}} \right)}{\beta - 1 + \left(\frac{\varepsilon_c}{\varepsilon_{c0}} \right)^{\beta}} \right], \tag{1}$$

$$\sigma_t = \begin{cases} f_t \left[1.2 \frac{\varepsilon_t}{\varepsilon_{to}} - 0.2 \left(\frac{\varepsilon_t}{\varepsilon_{to}} \right)^6 \right] & 0 \le \varepsilon_t \le \varepsilon_{to} \\ f_t \left[\frac{\frac{\varepsilon_c}{\varepsilon_0}}{1.25 \left(\frac{\varepsilon_t}{\varepsilon_{to}} - 1 \right)^2 - \frac{\varepsilon_t}{\varepsilon_{to}}} \right] & \varepsilon_{to} < \varepsilon_t \end{cases} \tag{2}$$

In these equations, σ_c represents the concrete stress, while ε_c corresponds to its strain. Parameters f_c and ε_{c0} denote the concrete compressive strength and the compressive strain at peak stress, respectively. Moreover, the variable β, reliant on the stress–strain curve's shape, was calculated using Eq. 3 (Nataraja et al., 1999):

$$\beta = \left(\frac{f_c}{32.4} \right) + 1.55. \tag{3}$$

Based on previous studies, the current relationship gained a well prediction of the compressive behavior of NC as previously recommended (Hamoda et al., 2019,

2024a, 2024b). This standardization ensures accurately capturing the performance of HSFRC and ECC and provides a realistic representation of its response under various loading conditions (Sarkar et al., 2023; Yehia et al., 2023). Moreover, the steel properties have been modeled through the idealized stress–strain response as presented in Fig. 4 as previously followed (Hamoda & Hossain, 2019; Hamoda et al., 2023b, 2024b). According to several attempts, the mentioned sensitive parameters and smooth stress–strain exhibition showed the most economic computational cost could closely simulate the edge RC columns as laterally verified. This modeling approach accurately captured the response of the steel elements under varying loads and deformations.

4.3 Sensitivity of Numerical CDP Parameters

In the pursuit of achieving a meticulously calibrated numerical model with precisely defined constitutive parameters, the current FEM underwent multiple iterations. The objective was to highlight the sensitivity of three crucial numerical factors: mesh size (l), dilation angle (ψ), and viscosity parameter (μ). Five trial FEMs have been attempted with mesh size varying from 10 mm up to 30 mm as shown in Fig. 15a. However, it was illustrated that the model with 20 mm mesh size was the best economic model with lower running cost could gain acceptable results as confirmed previously (Hamoda et al., 2019, 2021, 2023a, 2024a). In these sensitivity analyses, as illustrated in Fig. 15, the baseline FEM was configured with a mesh size of 20 mm, striking a balance between computational efficiency and reliability compared to other rivals. This choice offered a satisfactory outcome, providing a reasonably precise solution without escalating computational expenses. Again, some FEMs were executed considering different dilation angle as shown in Fig. 15b. However, it was emphasized that the dilation angle was meticulously set at 20 for NC, and at 30 for both ECC and HPFRC, ensuring a nuanced exploration of their impact on the overall model as previously confirmed (Hamoda et al., 2021, 2023a, 2023b). The viscosity parameter was established at 0.001 parallel to some previous studies (Hamoda et al., 2019, 2024a, 2024b).

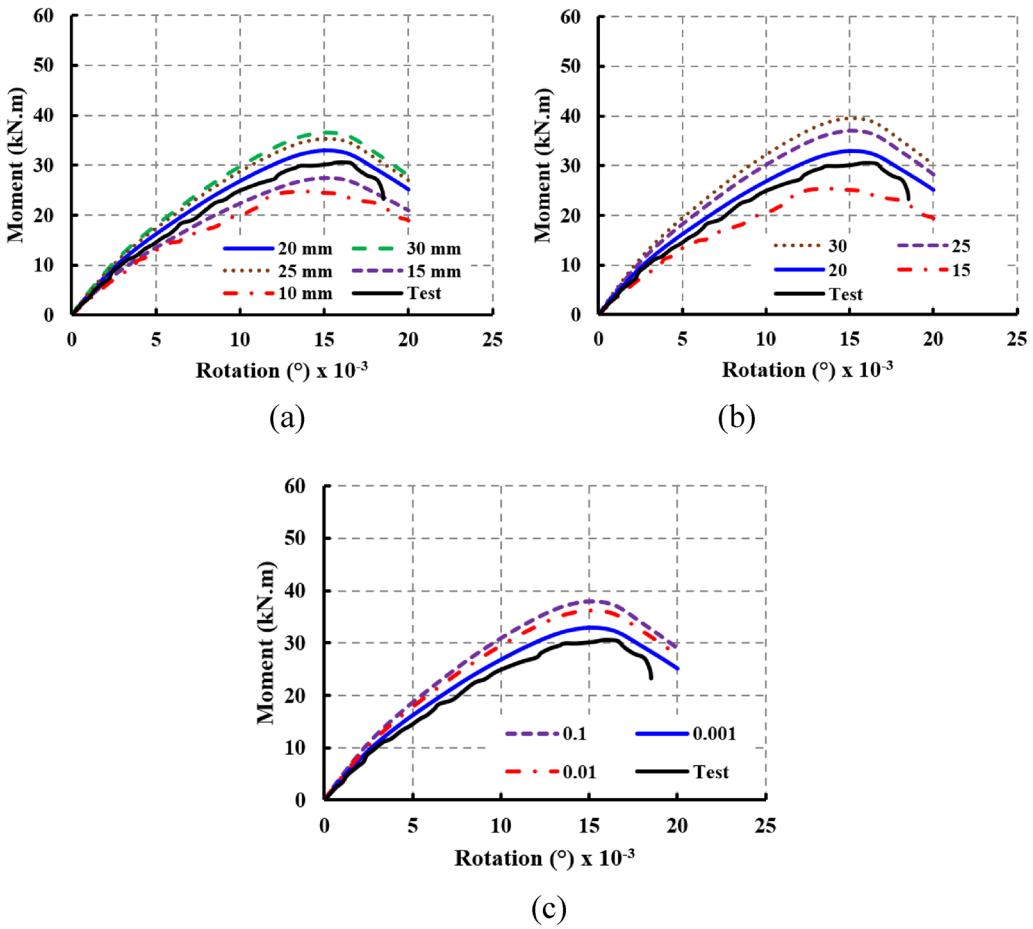

Fig. 15 Sensitivity analysis results: **a** mesh size; **b** dilation angle; and **c** viscosity parameter

Moreover, this value provided better results compared to those with higher values as it can be seen in Fig. 15c.

4.4 FEM Verification

Four FEMs were selected from each group to be compared and validated against experimental observation; those were: NC-2.2-200, NC-2.6-200, NC-2.2-167 and NC-2.2-200-L2. The results were validated and compared against experimental data in terms of: the load–deflection relationship, cracking visualization, cracking, yield and ultimate stages. The load–rotation responses observed experimentally and numerically are shown in Fig. 16, while the cracking visualizations are shown in Fig. 17. To ensure thorough verification, Table 5 was used to compare the FEM results with the corresponding experimental data in terms of cracking, yield and ultimate stages.

The observations shown in Fig. 16 illustrated that the built FEM rigorously anticipated cracking and ultimate levels, elastic and plastic exhibition, along with deformation throughout all stages. The CDP model has been previously employed for modeling the elastic–plastic concrete performance up to failure (Emara et al., 2023; Kim et al., 2024; Liu et al., 2020; Mostafa, 2024). The verification presented that the CDP could perfectly capture the right failure mode observed experimentally as shown in Fig. 17. Also, as shown in Fig. 17, the executed model remarkably predicted the different failure modes and formation of crack patterns obtained experimentally. In this context, the generation of the half-oval shape captured experimentally has been visualized numerically as remarked in Fig. 17. The installed FEM estimated well the experimental ultimate load capacity values as shown in Table 5 with an error of about 3%. However, this error might be decreased with specific testing of the material properties and several executed models in order to better capturing the structural performance of such columns. The mean value for ratios of $M_{\text{cr FE}}/M_{\text{cr EXP}}$, $M_{y\text{ FE}}/M_{y\text{ EXP}}$ and $M_{u\text{ FE}}/M_{u\text{ EXP}}$ are 1.049, 0.963 and 0.98 with standard deviation (SD) of 0.047, 0.015 and 0.038 and coefficient of variation (COV) of about 0.0453, 0.0153 and 0.0384, respectively. Remarkably, the FEM accurately estimates the failure mode as well as the overall load–displacement behavior at all loading stages, indicating its reliability in capturing the structural response.

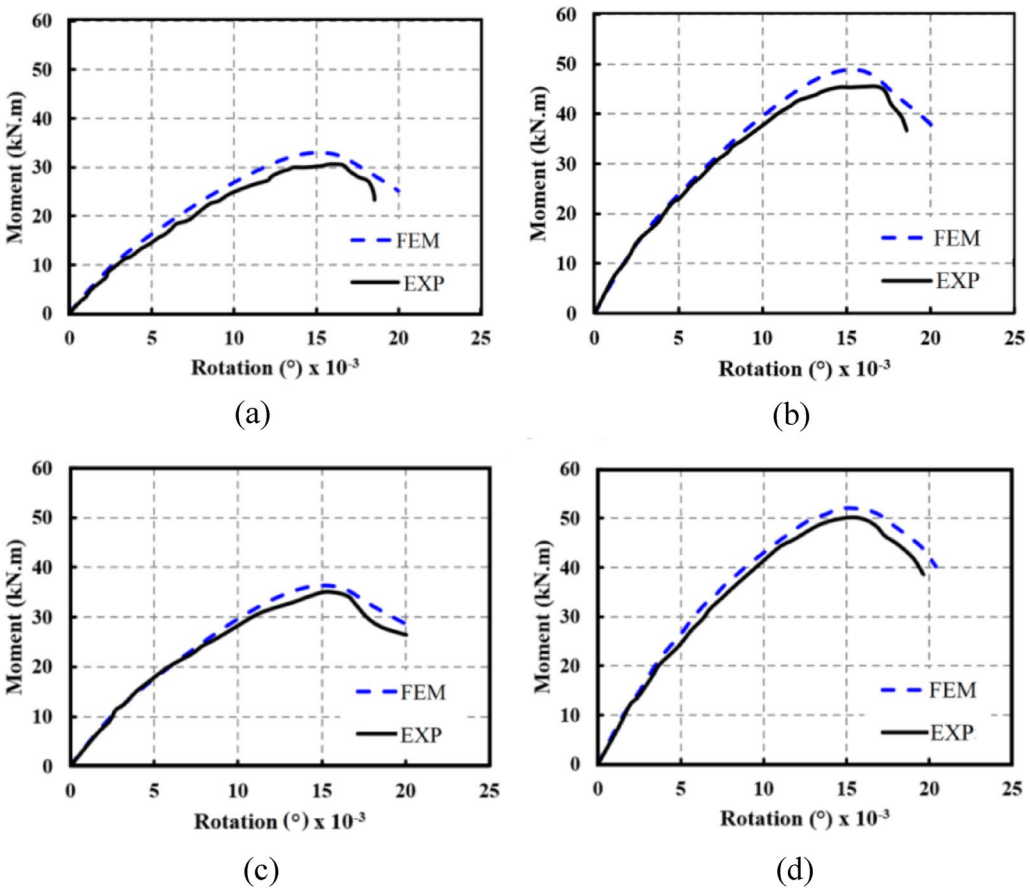

Fig. 16 Load–rotation response observed numerically and experimentally: **a** NC-2.2-200, **b** NC-2.6-200, **c** NC-2.2-167, and **d** NC-2.2-200-L2

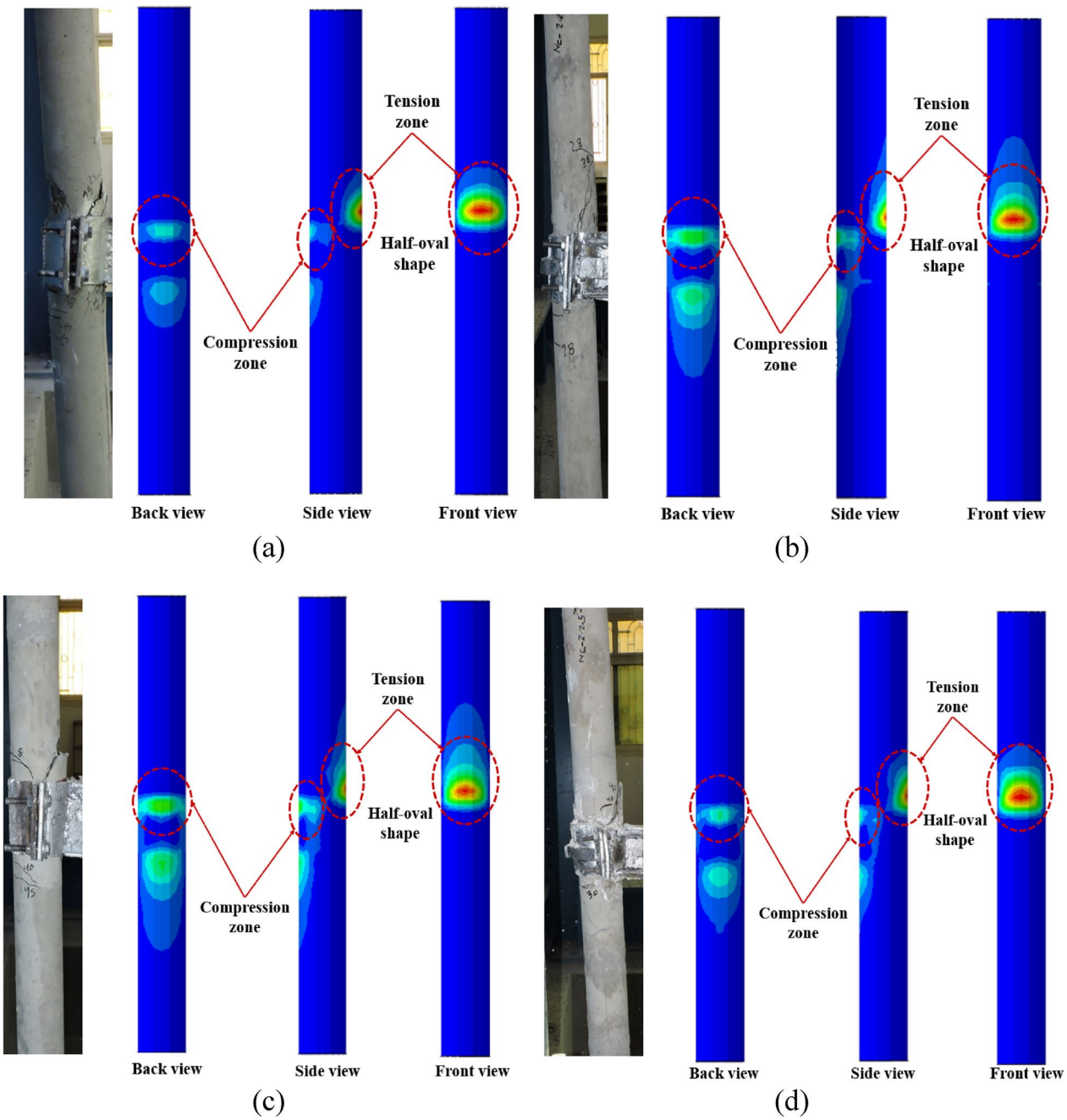

Fig. 17 Experimental and FE failure of selected specimens: **a** NC-2.2-200, **b** NC-2.6-200, **c** NC-2.2-167, and **d** NC-2.2-200-L2

5 Conclusions

This paper investigates experimentally and numerically the reflection of double curvature buckling edge moment transferred from beam–column to RC circular column. A total number of 11 full-scale RC circular columns were tested up to failure studying four factors. These parameters were: clear height-to-diameter ratio (λ), longitudinal and lateral steel ratios (ρ and μ, respectively) and along with concrete type. All columns were experimented under static monotonic moment at mid-height zone up to failure followed by numerical analysis. The following conclusions may be highlighted:

1. Test results illustrated that mostly such columns failed due to concrete crushing followed by dislocation of the elongated half-oval shape appeared at

Table 5 Experimental and numerical results

Specimen's ID	Cracking stage			Yield stage			Ultimate stage		
	M_{crEX} (kN)	M_{crFE} (kN)	FE/Ex	M_{yEX} (kN)	M_{yFE} (kN)	FE/Ex	M_{uEX} (kN)	M_{uFE} (kN)	FE/Ex
NC-2.2-200	7.42	7.31	0.98	24.46	23.21	0.95	30.58	29.90	0.98
NC-2.6-200	8.16	8.50	1.042	38.66	37.25	0.96	45.47	44.65	0.98
NC-2.2-167	9.07	9.85	1.086	30.31	28.97	0.96	35.06	36.36	1.03
NC-2.2-200-L2	9.57	10.38	1.084	36.27	35.65	0.98	50.07	49.22	0.98
Error									3%
Avg			1.049			0.963			0.98
SD			0.047			0.015			0.038
COV			0.0453			0.0153			0.0384

the flexural tension region. Such mode of failure has been established from numerical simulation.

2. The parameter of longitudinal reinforcement ratio provided better augmentation to both the ultimate capacity and absorbed energy in particular with ratio ranged in between 2.3% and 3.1%, since test results revealed that the ultimate capacity and absorbed energy have been increased within range of 27%–51%, and 39%–74%, respectively.
3. The contribution of ECC and HSFRC enhanced the cracking stage, elastic stiffness, ultimate capacity and the absorbed energy by about 40% and 45%, 20% and 34%, 19% and 25%, beside 33% and 34%, respectively, compared to ordinary type.
4. The lateral reinforcement delivered with 1.18% ratio increased the cracking and ultimate stages by about 26% for both, while about 41% increase was detected for absorbed energy. However, the use of lower ratios of stirrups with 0.93% or 1% presented undesirable contribution into the recorded values of structural results (only about 15% upgrading the ultimate load).
5. The installed model could accurately exemplify well RC circular columns subjected to double curvature moment, assessing the structural performance and predicting ultimate loads of RC circular columns subjected to double curvature moment the with an error of 3%. Therefore, the FEM can be utilized to implement future parametric studies.

Acknowledgements
The help from technicians at Kafrelsheikh University in performing the tests is acknowledged. The authors declare that this work has been funded by themselves.

Author contributions
AH: Investigation, Data curation, Writing–original draft, Visualization, Writing - review & editing. SF:Investigation, Data curation, Writing–original draft, Visualization,Writing - review & editing. WM: Investigation, Datacuration, Writing–original draft, Visualization, Writing - review &editing. ME: Investigation, Data curation, Writing–original draft, Visualization, Writing - review & editing.

Funding
Open access funding provided by The Science, Technology & Innovation Funding Authority (STDF) in cooperation with The Egyptian Knowledge Bank (EKB).

Availability of data and materials
The experimental data can be obtained throughemail communication with the author at sabry_fayed@eng.kfs.edu.eg.

Received: 5 March 2024 Accepted: 26 June 2024
Published online: 11 October 2024

References

Abdelazim, W., Mohamed, H. M., Benmokrane, B., & Afifi, M. Z. (2020). Effect of critical test parameters on behavior of glass fiber-reinforced polymer-reinforced concrete slender columns under eccentric load. *ACI Structural Journal, 117*(4), 127–141.

Abdulla, N. A. (2020). Mechanical behavior of slender composite columns under axial compression load. *KSCE Journal of Civil Engineering, 24*(1), 208–218.

ACI Committee, 3. (2008). Building code requirements for structural concrete (ACI 318-08) and commentary. American Concrete Institute.

Afefy, H. M., & El-Tony, E.-T.M. (2016). Simplified design procedure for reinforced concrete columns based on equivalent column concept. *International Journal of Concrete Structures and Materials, 10*, 393–406.

Ahmed, M., Liang, Q. Q., Patel, V. I., & Hamoda, A. (2024). Inelastic analysis of octagonal concrete-filled steel tubular short columns under eccentric loading. *Structural Concrete*, *25*(2), 1418–1433.

Ahmed, M., Liang, Q. Q., Patel, V. I., Gohari, S., & Hamoda, A. (2023). Unified numerical model for performance analysis of various cross-sections of concrete-filled stainless-steel tubular stub columns under axial loading. In *Structures* (Vol. 55, pp. 799–817). Elsevier.

Alajarmeh, O., et al. (2020). Behavior of circular concrete columns reinforced with hollow composite sections and GFRP bars. *Marine Structures, 72*, 102785.

Al-Rousan, R. Z., & Barfed, M. H. (2019). Impact of curvature type on the behavior of slender reinforced concrete rectangular column confined with CFRP composite. *Composites Part b: Engineering, 173*, 106939.

Aules, W., Saeed, Y. M., & Rad, F. N. (2020). A novel anchorage system for strengthening slender RC columns with externally bonded CFRP composite sheets. *Construction and Building Materials, 245*, 118423.

Barua, S., Mahmoud, K., & El-Salakawy, E. (2021). Slender GFRP-RC circular columns under concentric, eccentric, and flexural loads: Experimental investigation. *Journal of Bridge Engineering, 26*(7), 04021033.

Carreira, D. J., & Chu, K.-H. (1985). Stress-strain relationship for plain concrete in compression. *Journal Proceedings, 82*(6), 797–804.

Chen, Z., Ning, F., Chen, J., Liu, X., & Xu, D. (2021). Test on mechanical behavior of SRC L-shaped columns under combined torsion and bending moment. *Earthquake Engineering and Engineering Vibration, 20*, 161–177.
Dharmaraj, R., et al. (2022). Investigation of reinforced concrete column containing metakaolin and fly ash cementitious materials. *Advances in Civil Engineering, 2022*, 1–13.
Du, P., Yang, Y., & Tan, K. H. (2022). Fire behaviour and design of hybrid fibre reinforced high-performance concrete columns subjected to uniaxial bending. *Engineering Structures, 251*, 113425.
El-Kholy, A. M., Abd El-Rahman, S. F., & El-Assaly, M. M. (2023). Short and long RC columns with internal WWM reinforcement under concentric and eccentric compression. *International Journal of Concrete Structures and Materials*, *17*(1), 10.
El-Shennawy, A., Boros, V., & Novak, B. (2013). Comparison between the provisions of the Egyptian code of practice and the eurocodes for reinforced concrete structures design. *Democratic Transition and Sustainable Communities*, 520.
Emara, M., Hamoda, A., & Hu, J. W. (2023). Numerical assessment of rectangular one-and two-way RC slabs strengthened with CFRP under impact loads. *Computers and Concrete, 31*(3), 173.
Ghoroubi, R., Mercimek, Ö., Özdemir, A., & Anil, Ö. (2020). Experimental investigation of damaged square short RC columns with low slenderness retrofitted by CFRP strips under axial load. In *Structures* (Vol. 28, pp. 170–180). Elsevier.
Guo, Y.-L., Geng, Y., & Qu, L.-Y. (2021). Time-dependent behaviour of circular steel tube confined reinforced concrete (STCRC) stub columns subjected to low axial load. *Engineering Structures, 243*, 112663.
Hamoda, A. A., Ahmed, M., Abadel, A. A., Ghalla, M., Patel, V. I., & Liang, Q. Q. (2023). Experimental and numerical studies of circular precast concrete slender columns with intermediate connection filled with high-performance concrete. In *Structures* (Vol. 57, p. 105–204). Elsevier.
Hamoda, A., Emara, M., Abadel, A. A., & Sennah, K. (2024). Influence of shear strengthening of reinforced normal concrete beams incorporating sustainable materials. *Structural Concrete*.
Hamoda, A., Shahin, R. I., Ahmed, M., Abadel, A. A., Baktheer, A., & Yehia, S. A. (2024, June). Strengthening of reinforced concrete columns incorporating different configurations of stainless-steel plates. In *Structures* (Vol. 64, p. 106577). Elsevier.
Hamoda, A., Abdelazeem, F., & Emara, M. (2021). Concentric compressive behavior of hybrid concrete–stainless steel double-skin tubular columns incorporating high performance concretes. *Thin-Walled Structures, 159*, 107297.
Hamoda, A., Ahmed, M., Ghalla, M., Liang, Q. Q., & Abadel, A. A. (2023a). Flexural performance of precast circular reinforced concrete members with intermediate connection filled with ultra-high-performance-concrete. *Case Studies in Construction Materials, 19*, e02386.
Hamoda, A., Emara, M., & Mansour, W. (2019). Behavior of steel I-beam embedded in normal and steel fiber reinforced concrete incorporating demountable bolted connectors. *Composites Part b: Engineering, 174*, 106996.
Hamoda, A., & Hossain, K. (2019). Numerical assessment of slab–column connection additionally reinforced with steel and CFRP bars. *Arabian Journal for Science and Engineering, 44*, 8181–8204.
Hou, C., Zheng, W., Liu, P., Wang, Q., & Qi, S. (2023). Seismic performance of concrete columns confined by high-strength stirrups. *Archives of Civil and Mechanical Engineering, 23*(2), 69.
Jin, L., Zhang, S., Li, D., Xu, H., Du, X., & Li, Z. (2018). A combined experimental and numerical analysis on the seismic behavior of short reinforced concrete columns with different structural sizes and axial compression ratios. *International Journal of Damage Mechanics, 27*(9), 1416–1447.
Ju, S., & Kwak, H.-G. (2021). Moment-curvature approach for blast analysis of RC frames with multitudinous members. *Journal of Building Engineering, 42*, 102463.
Kharal, Z., & Sheikh, S. A. (2020). Seismic behavior of square and circular concrete columns with GFRP reinforcement. *Journal of Composites for Construction, 24*(1), 04019059.
Kim, S., Jeong, Y., Kwon, M., & Kim, J. (2024). Experimental and Numerical Study on the Behavior of RC Members under Combined Loads. *International Journal of Concrete Structures and Materials, 18*(1), 1–17.
Lamberti, M., & Razaqpur, G. (2024). A new method for rapidly capturing the strength and full nonlinear response of partially interacting steel–concrete composite beams. *Composites Part C: Open Access*, *14*, 100467.
Li, X., Wang, X., Liu, J., & Chen, Y. F. (2023). Behavior and design of eccentrically-loaded slender tubed steel-reinforced high-strength concrete columns. *Journal of Constructional Steel Research, 205*, 107907.
Lin, S., Li, Z., Lu, Z.-H., & Zhao, Y.-G. (2022). Experimental study on the behavior of circular ultra-high strength concrete-filled steel tube columns subjected to unequal end moments. *Engineering Structures, 267*, 114709.
Liu, S., Wang, X., Ali, Y. M., Huang, H., Zhou, J., & Wu, Z. (2023). Experimental study on eccentric compression behavior of slender rectangular concrete columns reinforced with steel and BFRP bars. *Engineering Structures, 293*, 116626.
Liu, T., Lu, J., & Liu, H. (2020). Experimental and numerical studies on the mechanical performance of a wall-beam-strut joint with mechanical couplers for prefabricated underground construction. *International Journal of Concrete Structures and Materials, 14*, 1–23.
Mostafa, M. M. (2024). Numerical FE modeling and design methods of CCES columns with normal-weight crushed dolomite coarse aggregate fully embedded IPE steel-section. *International Journal of Concrete Structures and Materials, 18*(1), 7.
Nataraja, M., Dhang, N., & Gupta, A. (1999). Stress–strain curves for steel-fiber reinforced concrete under compression. *Cement and Concrete Composites, 21*(5–6), 383–390.
Rivera, J. E., Eid, R., & Paultre, P. (2021). Influence of synthetic fibers on the seismic behavior of reinforced-concrete circular columns. *Engineering Structures, 228*, 111493.
Sae-Long, W., Limkatanyu, S., Prachasaree, W., Horpibulsuk, S., & Panedpojaman, P. (2019). Nonlinear frame element with shear–flexure interaction for seismic analysis of non-ductile reinforced concrete columns. *International Journal of Concrete Structures and Materials, 13*, 1–19.
Sarkar, S., Chakraborty, S., & Nayak, S. (2023). Identification of optimum reinforcement detailing using tuned CDP parameters in RC beam under drop-weight impact. *Engineering Failure Analysis*, *146*, 107116.
Štefan, R., Sura, J., Procházka, J., Kohoutková, A., & Wald, F. (2019). Numerical investigation of slender reinforced concrete and steel–concrete composite columns at normal and high temperatures using sectional analysis and moment-curvature approach. *Engineering Structures, 190*, 285–305.
Taherirani, M., Noroozolyaee, M., Salimian, M. S., & Mostofinejad, D. (2022). Evaluation of square slender RC columns subjected to eccentric loading strengthened with longitudinal FRP sheets based on PIV analysis. *Construction and Building Materials, 324*, 126635.
Teoh, K. B., Chua, Y. S., Dai Pang, S., & Kong, S. Y. (2023). Experimental investigation of flexural buckling behaviour of self-compacting lightweight concrete-filled cold-formed built-up box section (CFBBS) columns. *Thin-Walled Structures, 187*, 110751.
Ye, J. B., Cai, J., Chen, Q. J., Liu, X., Tang, X. L., & Zuo, Z. L. (2020). Experimental investigation of slender RC columns under horizontal static and impact loads. In *Structures* (Vol. 24, pp. 499–513). Elsevier.
Yehia, E., Khalil, A. H., Mostafa, E. E., & El-Nazzer, M. A. (2023). Experimental and numerical investigation on punching behavior of ultra-high performance concrete flat slabs. *Ain Shams Engineering Journal*, *14*(10), 102208.
Zhou, J., Chen, Z., Liu, D., Qin, W., & Li, J. (2023, November). Experimental and numerical investigations on eccentric compression behavior of square CFST columns with inner spiral stirrup. In *Structures* (Vol. 57, p. 105196). Elsevier.

Publisher's Note

Ahmed Hamoda Associate Professor, Department of Civil Engineering, Faculty of Engineering, Kafrelsheikh University, Kafrelsheikh, Egypt.

Sabry Fayed Associate Professor, Department of Civil Engineering, Faculty of Engineering, Kafrelsheikh University, Kafrelsheikh, Egypt.

Walid Mansour Assistant Professor, Department of Civil Engineering, Faculty of Engineering, Kafrelsheikh University, Kafrelsheikh, Egypt.

Mohamed Emara Structural Engineering Department, Faculty of Engineering, Zagazig University, B.O. Box 44519, Zagazig, Sharkia, Egypt. Department of Civil Engineering, Delta Higher Institute for Engineering & Technology, Talkha, Egypt.